PHYSICAL REVIEW E **109**, 045101 (2024)

Connecting finite-time Lyapunov exponents with supersaturation and droplet dynamics in a turbulent bulk flow

Vladyslav Pushenko and Jörg Schumacher
Institut für Thermo- und Fluiddynamik, Technische Universität Ilmenau, Postfach 100565, D-98684 Ilmenau, Germany

(Received 25 January 2024; accepted 26 February 2024; published 1 April 2024)

The impact of turbulent mixing on an ensemble of initially monodisperse water droplets is studied in a turbulent bulk that serves as a simplified setup for the interior of a turbulent ice-free cloud. A mixing model was implemented that summarizes the balance equations of water vapor mixing ratio and temperature to an effective advection-diffusion equation for the supersaturation field $s(\boldsymbol{x},t)$. Our three-dimensional direct numerical simulations connect the velocity and scalar supersaturation fields in the Eulerian frame of reference to an ensemble of cloud droplets in the Lagrangian frame of reference. The droplets are modeled as point particles with and without effects due to inertia. The droplet radius is subject to growth by vapor diffusion. We report the dependence of the droplet size distribution on the box size, initial droplet radius, and the strength of the updraft, with and without gravitational settling. In addition, the three finite-time Lyapunov exponents $\lambda_1 \geqslant \lambda_2 \geqslant \lambda_3$ are monitored which probe the local stretching properties along the particle tracks. In this way, we can relate regions of higher compressive strain to those of high local supersaturation amplitudes. For the present parameter range, the mixing process in terms of the droplet evaporation is always homogeneous, while it is inhomogeneous with respect to the relaxation of the supersaturation field. The probability density function of the third finite-time Lyapunov exponent, $\lambda_3 < 0$, is related to the one of the supersaturation s by a simple one-dimensional aggregation model. The probability density function (PDF) of λ_3 and the droplet radius r are found to be Gaussian, while the PDF of the supersaturation field shows sub-Gaussian tails.

DOI: 10.1103/PhysRevE.109.045101

I. INTRODUCTION

Atmospheric clouds are complex physical systems that play a key role in synoptic timescales for the formation of precipitation [1] and in much longer timescales for the radiation budget of the climate of our planet [2]. The water appears in different phases inside a cloud, either as water vapor, liquid water droplets, or ice crystals. All phases affect the optical properties of clouds crucially; the overall turbulent dynamics determines the local increase and decrease of the corresponding mixing ratios [3,4]. Warm ice-free clouds form a two-component turbulent multiphase flow (water and vapor). The cloud water droplet number density and size distribution are then two key quantities in view to rain formation for which droplets typically have to grow up to about 1 mm. One of the central questions remains how the turbulent mixing of dry air and moist air, in particular entrainment [5,6], alters the number density and size distribution of cloud water droplets inside the cloud, and which role the locally fluctuating supersaturation does play; see, e.g., Refs. [7–15] for numerical investigations inside clouds or at their edges.

These questions provide the central motivation for the present study. Here, we discuss a strongly simplified model of turbulent mixing in the bulk of a cloud by means of three-dimensional direct numerical simulations (DNSs). This simplification consists of a summary of the balance equations for the Eulerian fields of vapor mixing ratio and temperature, $q_v(\boldsymbol{x},t)$ and $T(\boldsymbol{x},t)$, to an effective balance equation for the scalar supersaturation field, following Refs. [9,10,16,17]. We assume that the supersaturation field $s(\boldsymbol{x},t)$ does not act back on the flow; it is thus a passive scalar field in the present approach. The field is given by

$$s(\boldsymbol{x},t) = \frac{q_v(\boldsymbol{x},t)}{q_{vs}(T)} - 1, \tag{1}$$

with the saturation mixing ratio q_{vs} of vapor which depends on temperature T via the Clausius-Clapeyron equation [18]. This field determines the diffusion growth of an ensemble of individual Lagrangian cloud water droplets which are considered pointlike particles with an attached radius coordinate. In the present work, we connect the statistics of finite-time Lyapunov exponents of the advecting velocity field [19], which quantify the local stretching and compression rates in the Lagrangian frame of reference, to the statistics of $s(\boldsymbol{x},t)$ and thus to the droplet size (or droplet radius) distribution. A further simplification of the present model is that the droplets are subject to a one-way coupling only. Götzfried *et al.* [20] showed that the particle Reynolds number for the initial radii, which are taken here, remain smaller. An objective of our approach is to test an aggregation model of the turbulent mixing of passive scalar fields, which has been successfully applied for turbulent mixing at high Schmidt numbers Sc in the past [21–23]. The scalar statistics is followed then by a successive stretch-twist-fold stirring of scalar concentration filaments that are subject to molecular diffusion. We report current results for a small cubical reference volume in the bulk of a cloud where a Schmidt number Sc ≈ 0.7 is considered for the scalar supersaturation field $s(\boldsymbol{x},t)$. As already said, this is significantly smaller than the ones in Refs. [21,22,24,25].

We find that the supersaturation dynamics is then Gaussian-distributed in the core with sub-Gaussian tails, both from the Eulerian statistical analysis as well as along the individual droplet trajectories. This causes Gaussian-shaped droplet size distributions, which broaden faster when the box size becomes bigger.

Turbulent mixing, particularly across the boundary of a cloud, influences the number density and size distribution of cloud droplets by causing fluctuations of water vapor and liquid water content, as we showed in previous works [20, 26–29], partly in significantly more complex configurations with several nonlinear feedbacks. Here, we focus on the simpler mixing inside the cloud bulk. Mixing can be characterized by Damköhler number Da [30,31], the ratio of the typical flow timescale, such as the large-scale eddy turnover time to a characteristic thermodynamic reaction timescale of interest,

$$\mathrm{Da} = \frac{\tau_L}{\tau_{\mathrm{react}}}. \tag{2}$$

Thermodynamic processes, which are characterized by small Damköhler numbers (Da $\ll 1$), proceed slower than the flow is mixed; this mixing regime is called thermodynamics-limited or *homogeneous*; see, e.g., Ref. [32]. For cloud droplet evaporation, it means that moist air will be properly mixed, and droplets will evaporate at approximately the same rate. In the regime with the large Damköhler number (Da $\gg 1$), the corresponding thermodynamic regime is called mixing-limited or *inhomogeneous*. In this regime, the moist air is mixed slower by the flow than it is saturated by evaporating droplets. For inhomogeneous mixing, cloud droplets evaporate in different regions with different rates [17,27,33,34]. As was shown in [27], the inhomogeneous mixing gives extended tails of the cloud droplet size distribution. Higher levels of fluctuations of water vapor content in different regions generate different rates of growth and shrinkage of cloud water droplets. We want to investigate how strong this variability of the droplet radius r is in the bulk of a cloud.

The paper is organized as follows. In Sec. II, we provide the cloud mixing model, define the main parameters of our model, and discuss their influence on the mixing processes. Section III discusses DNS results obtained from the turbulence fields in the Eulerian frame of reference. Section IV is dedicated to the Lagrangian analysis of the cloud water droplets. While Sec. IV A discusses the Lagrangian tracer case, Sec. IV B investigates the effects of gravity and the initial radius on the droplet dynamics. The definition of finite-time Lyapunov exponents (FTLEs) is provided in Sec. V. Here, we connect these results to those of the previous sections before a summary and outlook is given in Sec. VI. The Appendix provides the derivation of the effective advection-diffusion equation for the supersaturation field for completeness.

II. NUMERICAL SIMULATION MODEL

A. Eulerian and Lagrangian model equations

In our cloud mixing model, we consider a subvolume $V = L^3$ in the bulk of a cloud as a multiphase system that consists of dry air, water vapor, and liquid water. We assume periodic boundary conditions in all three directions. The turbulent velocity field $\boldsymbol{u}(\boldsymbol{x}, t)$ is assumed to be statistically stationary, homogeneous, and isotropic. The full complexity of the mixing process in the presence of phase changes requires balance equations for the (i) temperature field $T(\boldsymbol{x}, t)$ including latent heat release, (ii) vapor mixing ratio $q_v(\boldsymbol{x}, t)$ including condensation rate as a loss term, and (iii) liquid water mixing ratio $q_l(\boldsymbol{x}, t)$ including condensation rate as a gain term.

The models of Celani *et al.* [8,16], Sardina *et al.* [10], and Fries *et al.* [17] simplify this complex dynamics in three aspects. First, the liquid water content is represented by an ensemble of individual spherical pointlike cloud water droplets. Attached is a droplet radius that can increase and decrease, thus changing q_l. Second, the fields T and q_v are summarized in the scalar supersaturation field $s(\boldsymbol{x}, t)$. Third, the mixing of the scalar field and the advection of the droplets will not couple back to the turbulent velocity field $\boldsymbol{u}(\boldsymbol{x}, t)$ via a buoyancy term, i.e., there is a one-way coupling considered only. This assumption is justified when the droplet radii remain small and the droplet number density $n_0 \sim 100\,\mathrm{cm}^{-3}$ as in our study. The Eulerian equations of motion follow as

$$\nabla \cdot \boldsymbol{u} = \boldsymbol{0}, \tag{3a}$$

$$\frac{\partial \boldsymbol{u}}{\partial t} + (\boldsymbol{u} \cdot \nabla)\boldsymbol{u} = -\frac{\nabla p}{\rho} + \nu \nabla^2 \boldsymbol{u} + \boldsymbol{f}, \tag{3b}$$

$$\frac{\partial s}{\partial t} + (\boldsymbol{u} \cdot \nabla)s = D_s \nabla^2 s + A_1 u_z - A_2 \frac{4\pi \rho_L K'}{V_a} \times \sum_{i=1}^{N} r_i(t) s(\boldsymbol{X}_i, t). \tag{3c}$$

Due to its small size, cloud water droplets will have a small Stokes number (St $\ll 1$) and are thus approximated as Lagrangian tracer particles without inertia following perfectly the streamlines of the turbulent velocity field for most of the work, except in Sec. IV B. In Ref. [26], we showed that effects of additional droplet inertia for the presently chosen parameters remain small. The dynamics of the n_p individual cloud water droplets is given by [18]

$$\frac{d\boldsymbol{X}_i}{dt} = \boldsymbol{u}(\boldsymbol{X}_i, t), \quad i = 1, \dots, n_p, \tag{4a}$$

$$r_i \frac{dr_i}{dt} = K' s(\boldsymbol{X}_i, t). \tag{4b}$$

The coefficients in the combined Euler-Lagrangian model equations depend on thermodynamic properties of the cloud. They are defined as

$$A_1 = \frac{\mathcal{L} g}{R_v c_p T^2}, \tag{5a}$$

$$A_2 = \frac{R' T}{\varepsilon e_s(T)} + \frac{\mathcal{L}^2 \varepsilon}{p T c_p}, \tag{5b}$$

$$K' = \left[\frac{\mathcal{L} \rho_l}{k T} \left(\frac{\mathcal{L}}{R_v T} - 1 \right) + \frac{\rho_l R_v T}{D e_s(T)} \right]^{-1}. \tag{5c}$$

Here $p(\boldsymbol{x}_i, t)$ is the pressure field, and ρ is the constant fluid density. Quantities $r_i(t)$ and $\boldsymbol{X}_i(t)$ are the radius and the spatial position for the ith cloud water droplet, respectively. Furthermore, ν is the kinematic viscosity, $\boldsymbol{f}(\boldsymbol{x}, t)$ is the large-scale volume forcing of the flow, D_s is the diffusion coefficient of the supersaturation field, $\mathcal{L}$ is the latent heat of evaporation, g is the acceleration due to gravity, R_v is the gas constant for water vapor, c_p is the specific heat at constant pressure, R' is the gas constant of dry air, $\varepsilon = R'/R_v$ is the ratio of both gas constants, $e_s(T)$ is the saturation water vapor pressure, and ρ_l is the density of liquid water. Also, k is the thermal conductivity of air, D is the diffusion coefficient of the water vapor diffusion, V_a is the grid cell volume, and N is the number of particles in the vicinity of the grid cell volume around position $\boldsymbol{x}$.

The diffusion coefficient of the supersaturation field, D_s, can be well approximated by the diffusion coefficient of water vapor, D [10]. The first of the two forcing terms, $A_1 u_z$, in Eq. (3c) is due to the temperature gradient in the z-direction. For the present box sizes, the prefactor turns out to be very small with $O(10^{-3})$. Thus we have enhanced this factor in the first three runs, and we discuss the realistic magnitude in Sec. IV B. The second term in Eq. (3c) is a condensation rate term, i.e., a change of the liquid water content in the air slab. It quantifies the effects of condensation and evaporation and thus couples the dynamics of the scalar field and the cloud droplets. In turn, their individual radius changes with variations of the supersaturation field [18]. In the Appendix, we provide the detailed derivation of Eq. (3c) for completeness; see also [10,17,35].

B. Dimensionless form of equations and parameters

We set the same initial radius r_0 for all droplets and seed them randomly across the whole computational domain. To get the dimensionless equations out of (4), the following characteristic scales are chosen. The root mean square of the velocity field is $U = \sqrt{2E_k}$, where $E_k = \frac{1}{2}\langle u_i^2\rangle_{V,t}$ is the turbulent kinetic energy. As the characteristic timescale, the large-eddy turnover time $\tau_L = E_k/\langle\epsilon\rangle_{V,t}$ is chosen. Here $\epsilon = 2\nu S_{ij}S_{ij}$ is a turbulent energy dissipation rate, where $S_{ij} = (\partial_j u_i + \partial_i u_j)/2$ is the rate-of-strain tensor. The characteristic passive scalar scale is the root mean square of the supersaturation, $s_{\rm rms} = \langle s^2\rangle_{V,t}$. Note that the supersaturation field is kept in a statistically stationary state. Here, $\langle\cdot\rangle_{V,t}$ is a combined average with respect to volume and time. The initial droplet radius is r_0, the corresponding number density is n_0. Using these assumptions, the dimensionless versions of (3) and (4) are given by

$$\nabla\cdot\boldsymbol{u} = \boldsymbol{0}, \tag{6a}$$

$$\frac{\partial\boldsymbol{u}}{\partial t} + (\boldsymbol{u}\cdot\nabla)\boldsymbol{u} = -\nabla p + \frac{1}{\mathrm{Re}}\nabla^2\boldsymbol{u} + \boldsymbol{f}, \tag{6b}$$

$$\frac{\partial s}{\partial t} + (\boldsymbol{u}\cdot\nabla)s = \frac{1}{\mathrm{Re\,Sc}}\nabla^2 s + \tilde{A}_1 u_z + \mathrm{Da}_s V\sum_{i=1}^{N} r_i(t)s(\boldsymbol{X}_i,t), \tag{6c}$$

$$\frac{d\boldsymbol{X}_i}{dt} = \boldsymbol{u}(\boldsymbol{X}_i,t),\ \ i = 1,\dots,n_p, \tag{6d}$$

$$r_i\frac{dr_i}{dt} = \frac{\mathrm{Da}_d}{2}s(\boldsymbol{X}_i,t), \tag{6e}$$

with $\tilde{A}_1 = A_1 U/\tau_L$. From (6), the flow depends on the following nondimensional parameters: the large-scale Reynolds number Re, the Schmidt number Sc, and both Damköhler numbers, which are given by

$$\mathrm{Re} = \frac{U^2\tau_L}{\nu},\ \ \mathrm{Sc} = \frac{\nu}{D_s},\ \ \mathrm{Da}_s = \frac{\tau_L}{\tau_s},\ \ \mathrm{Da}_d = \frac{\tau_L}{\tau_d}. \tag{7}$$

These two Damköhler numbers have been identified in Refs. [30,31]. Here, τ_s is a supersaturation relaxation time, the timescale at which supersaturation will decay to saturation state; $\tau_{\rm d}$ is droplet evaporation time, which describes a timescale at which a droplet with initial radius r_0 should evaporate in a subsaturated environment with supersaturation magnitude $s = s_{\rm rms}$. The two timescales are determined by

$$\tau_s = \frac{1}{A_2 4\pi\rho_L K' r_0 n_0}, \tag{8a}$$

$$\tau_d = \frac{r_0^2}{2K' s_{\rm rms}}. \tag{8b}$$

When $\mathrm{Da}_d \ll 1$, the cloud droplets evaporate at approximately the same rate because the flow is well-mixed. The other regime with $\mathrm{Da}_d \gg 1$ implies that the droplets will have different rates of evaporation.

III. STATISTICS AND STRUCTURE OF THE EULERIAN TURBULENCE

The Eulerian equations of motion are solved by a standard pseudospectral direct numerical simulation. All fields are expanded in Fourier series; the switch between the physical and Fourier space is performed by fast Fourier transformations [36] using the software package P3DFFT [37]. The simulation domain is decomposed into pencils, and the simulation code is parallelized with the message passing interface. Time advancement is done by a second-order predictor-corrector scheme. The same time integration technique is used for tracking the Lagrangian tracer particles and calculating the Lyapunov exponents [23]. Interpolation to switch between Lagrangian and Eulerian descriptions is done trilinearly. We vary the Reynolds number and thus the degree of turbulent mixing by an increase of the box size L in the volume forcing term in the Navier-Stokes equations (3b). This forcing is defined such that at each time step a fixed amount of turbulent kinetic energy at a rate $\epsilon_{\rm in}$ is injected [36]. This term is implemented in the Fourier space,

$$\mathscr{F}\{\boldsymbol{f}(\boldsymbol{x},t)\} = \epsilon_{\rm in}\frac{\hat{\boldsymbol{u}}(\boldsymbol{k},t)}{\sum_{\boldsymbol{k}_f\in K}|\hat{\boldsymbol{u}}(\boldsymbol{k}_f,t)|^2}\delta_{\boldsymbol{k},\boldsymbol{k}_f}. \tag{9}$$

The subset of driven Fourier modes is given $K = \{\boldsymbol{k}_f = (2\pi/L)(\pm1,\pm1,\pm2)\}$ plus permutations of wave-vector components. Here, $\epsilon_{\rm in}$ is the energy injection rate that prescribes the dissipation of turbulent kinetic energy, i.e., $\epsilon_{\rm in} \approx \langle\epsilon\rangle_{V,t}$ for the statistically stationary regime. We performed three different DNSs to investigate how variations of L affect the flow properties. An additional parameter, which quantifies the strength of turbulence, is the Taylor microscale Reynolds number, which is listed in Table I. It is given by [36]

$$R_\lambda = \sqrt{\frac{5}{3\nu\langle\epsilon\rangle_{V,t}}}U^2. \tag{10}$$

Table I summarizes also other results. With increasing lengthscale L both Reynolds numbers and the velocity fluctuation

TABLE I. The parameters of the simulations with different domain sizes L and energy injection rates ϵ_{in}, numerical resolution as a ratio of bin size Δx to obtained Kolmogorov length scale η_K, number of grid-points in each direction n, number of particles n_p, coefficient of vertical ascending A_1, time- and volume-averaged root-mean-square velocity magnitudes U, large-scale eddy turnover times τ_L, and time- and volume-averaged root-mean-square supersaturation values s_{rms}. Furthermore, listed are Reynolds numbers Re, Taylor microscale Reynolds numbers R_λ, and the Damköhler numbers, Da_s and Da_d, specified for supersaturation and droplet evaporation, respectively. Quantities are given in their physical dimensions with amplitudes that correspond to typical conditions in a cloud.

Run	L (m)	ϵ_{in} (m^2/s^{-3})	$\frac{\Delta x}{\eta_K}$	n	n_p	A_1 (m^{-1})	U (m/s)	τ_L (s)	s_{rms}	Re	R_λ	Da_s	Da_d
1	0.128	0.0034	1.009	128	209 715	0.2	0.072	1.78	0.00439	614	28.4	1.04	0.0043
2	0.256	0.0034	1.006	256	1 677 721	0.2	0.097	2.64	0.00795	1655	51.6	1.54	0.0125
3	0.512	0.0034	1.002	512	13 421 772	0.2	0.129	3.97	0.01088	4406	72.9	1.85	0.5952

magnitude increase, as expected and shown in [29]. Consequently, the large-scale eddy turnover time τ_L grows as well. The values of $s_{\text{rms}} = \langle s^2 \rangle_{V,t}^{1/2}$ remain very small, but increase to about $\sim$1% for the biggest domain. We recall that in atmospheric clouds, heterogeneous nucleation proceeds such that maximum values of s typically do not exceed a few percent [18].

Figure 1 visualizes the turbulent dynamics by means of a slice-cut snapshot for runs 2 and 3 of Table I. On display are the velocity magnitude (or E_k) to the left, the passively mixed supersaturation field, and the logarithm of the kinetic energy dissipation field. It is clearly demonstrated how the complexity of the flow increases when the Reynolds number grows. The kinetic energy dissipation rate field develops finer striated high-amplitude shear layers. They are connected to stretching and compression regions in the Lagrangian picture which will be further investigated in Sec. V by means of the FTLEs.

Figure 2(a) demonstrates the probability density function (PDF) for a supersaturation field for run 2 which has Gaussian shape in the core and sub-Gaussian tails. This statistics agrees with passive scalar DNSs by Celani *et al.* [38]. Figure 2(b) displays isosurfaces of the instantaneous scalar dissipation rate field of the supersaturation. This quantity is given by

$$\epsilon_s(\boldsymbol{x}, t) = \frac{1}{\text{Re Sc}} [\nabla s(\boldsymbol{x}, t)]^2. \tag{11}$$

We see that the isosurfaces of the scalar dissipation rate at the chosen isolevel are mostly of smaller size, platelike, and not stretched out and curved, as would be the case for turbulent mixing at very large Schmidt numbers; see, e.g., Kushnir *et al.* [39]. The reason is that the chaotic stirring of the scalar at sub-Kolmogorov scales is absent for the present Schmidt number Sc $\sim$1. In other words, no viscous-convective range exists for the passive scalar in the present case which is established between the Kolmogorov length η_K and the diffusive length of the passive scalar, the Batchelor length $\eta_B = \eta_K/\sqrt{\text{Sc}}$. This will have implications for the prospective application of the aggregation model of passive scalars [21,22], which we will discuss further below in the text.

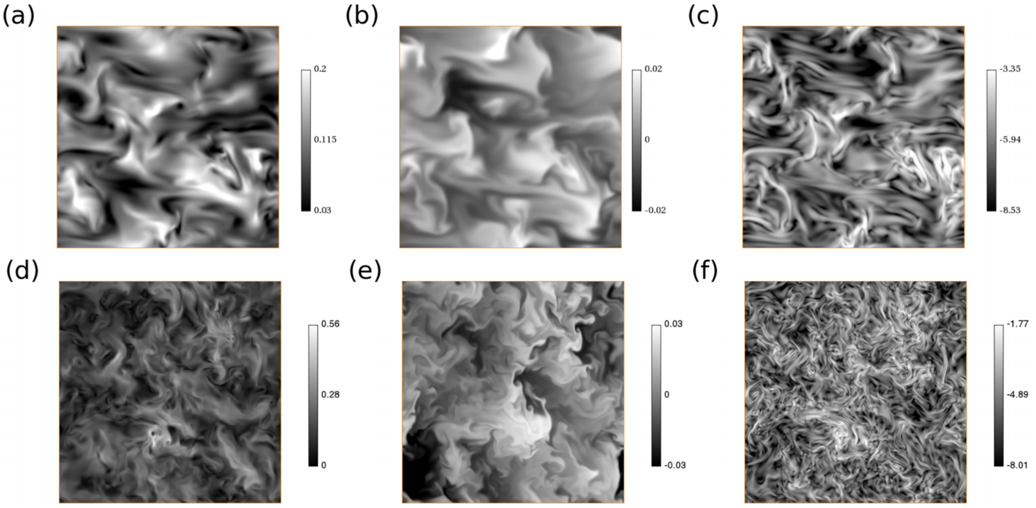

FIG. 1. Contour plots of two-dimensional slice cuts of (a) the magnitude of the velocity field, (b) the supersaturation field, and (c) the logarithm of the dissipation rate of turbulent kinetic energy. It is given by $\epsilon = 2\nu S_{ij} S_{ij}$, $S_{ij} = (\partial_j u_i + \partial_i u_j)/2$ with the rate-of-strain tensor S_{ij}. Data are for the simulation run 2 with $L = 256$ mm at $t = 0.045\tau_L$. The lower panels (d)–(f) show corresponding plots for simulation run 3 with $L = 512$ mm at $t = 0.032\tau_L$. See also Table I. The characteristic time unit, the large-scale eddy turnover time τ_L is specified in Sec. II B; see also Table I.

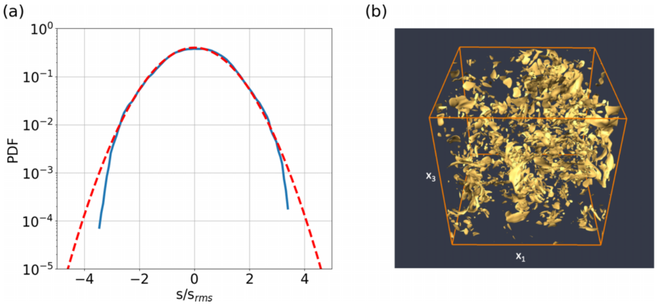

FIG. 2. (a) Sub-Gaussian PDF of rescaled supersaturation field taken from Eulerian approach (blue line) and Gaussian PDF for reference. (b) Instantaneous snapshot of isosurfaces of the scalar dissipation rate field $\epsilon_s(\boldsymbol{x}, t)$, which is defined in Eq. (11). The level of the isosurfaces is $\log_{10} \epsilon_s = -3.3$ in this plot.

IV. CLOUD WATER DROPLET DYNAMICS AND STATISTICS

A. Cloud water droplets as Lagrangian tracers

Each individual cloud water droplet was advected by statistically steady turbulent flow. It is seen from Eq. (4b) that the supersaturation field directly impacts the size distribution of cloud droplets. Figure 3 displays the droplet size distributions for runs 1, 2, and 3 taken at different time instants. The probability density function broadens in all cases with progressing time, but remains in a Gaussian shape without developing extended tails in the cloud bulk.

As seen in Table I, a larger domain size results in a larger velocity fluctuation magnitude. Consequently, the fluctuations of the supersaturation field are enhanced; see again Table I. As a consequence and as expected, the cloud droplet size distribution broadens much faster in time. Note that we provide the instants in terms of the corresponding large-scale eddy turnover timescale τ_L, which itself becomes larger as the domain size increases.

A more detailed analysis for individual cloud droplets was performed subsequently. Therefore, the Lagrangian droplets data of a few randomly selected particles, which are initially far enough separated from each other, were written out at each time integration step. The first plot of Fig. 4(a) demonstrates the variation of the droplet radius for two selected particles for a physical time of 2 min. The second plot of the figure in panel (b) shows the corresponding value of the supersaturation field $s(\boldsymbol{X}_p, t)$ at the particle position $\boldsymbol{X}_p(t)$. It can be clearly seen that time intervals with positive supersaturation ($s > 0$) correspond to the growth periods of cloud droplets. Droplets shrink in subsaturated air ($s < 0$) [16].

According to statistically steady homogeneous isotropic bulk turbulence, we expect that the PDF of $s(\boldsymbol{X}, t)$ converges to the Gaussian distribution in the core with sub-Gaussian tails. Particles which are advected in the turbulent volume are affected by differently long intervals of super- and subsaturation. Figure 4(c) confirms this point; we reproduce the Gaussian statistics in the core with the sub-Gaussian tails in the Lagrangian frame, which agrees consistently with the Eulerian analysis that was displayed in Fig. 2.

The evaporation and condensation processes of the cloud droplets depend on the character of corresponding mixing regime as shown in several field measurements and controlled laboratory experiments; see, e.g., Refs. [34,35,40]. As discussed already above in the Introduction, the mixing regime is defined by a Damköhler number. For cloud droplet evaporation, we take Da_d in (7). In the homogeneous mixing regime for $\mathrm{Da}_d \ll 1$, droplets evaporate with an almost equal rate, while in the inhomogeneous mixing regime evaporation rates of different droplets are different, i.e., some droplets can evaporate completely while others are not evaporated at all. Here, the cloud droplet evaporation is a homogeneous mixing process which explains the Gaussian distribution of the cloud droplet radii. The PDFs are without far-tails as they were seen in Ref. [28] for the edge of the cloud. The second thermodynamic process of interest, the saturation relaxation of the water vapour content, is parametrized by the

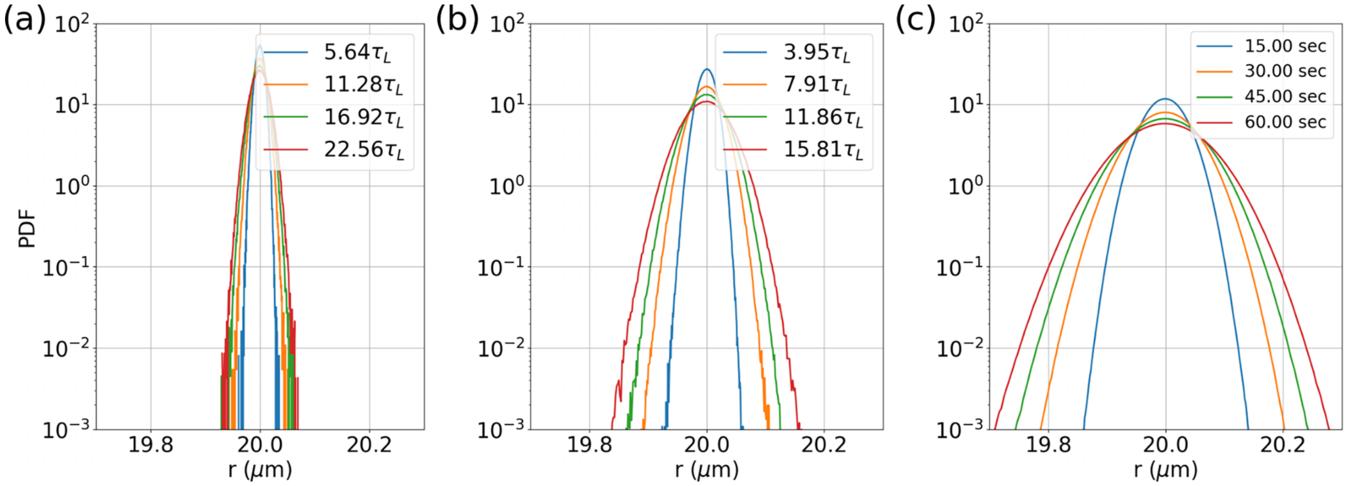

FIG. 3. Droplet size distribution at different time instants for computational domains with (a) $L = 128$ mm (run 1), (b) $L = 256$ mm (run 2), and (c) $L = 512$ mm (run 3). All times are expressed in units of the corresponding large-scale eddy turnover time τ_L which are provided in Table I.

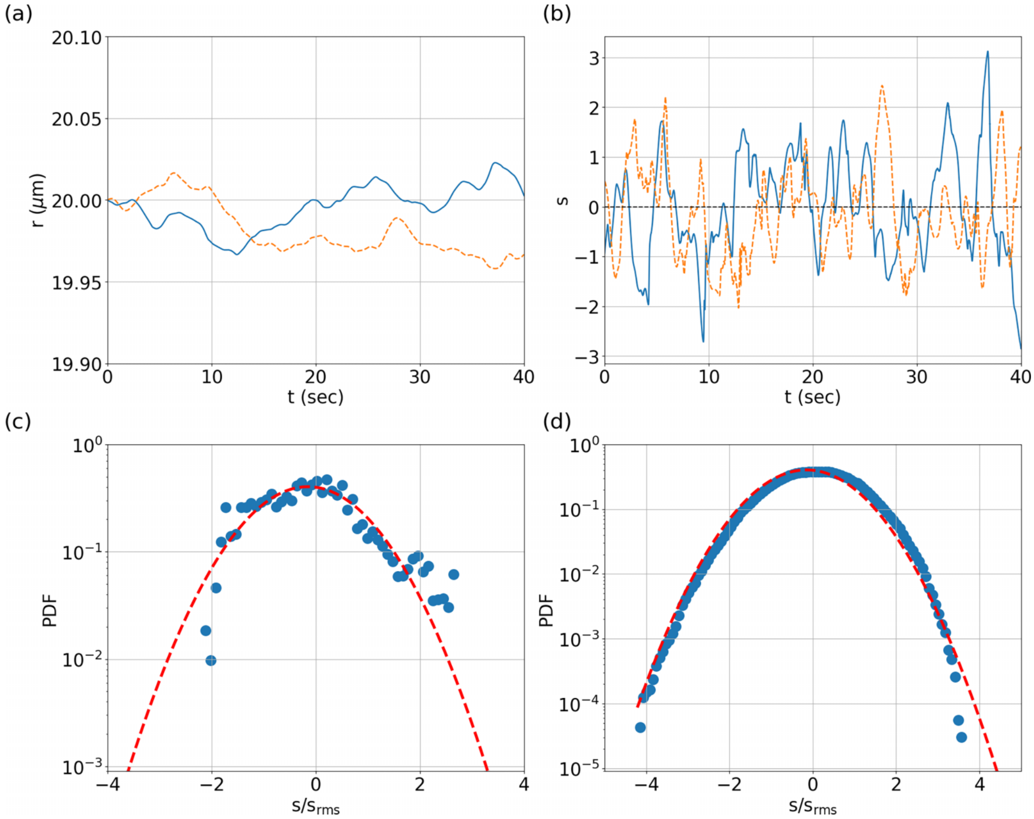

FIG. 4. Time evolution of two individual droplet radii in (a) and the corresponding supersaturation field in (b). Solid and dashed lines correspond to a particular particle. Time is given in seconds. (c) Probability density function (PDF) of the rescaled supersaturation field, $s/s_{\rm rms}$, experienced by the chosen individual particle for the whole calculation period, and (d) PDF of rescaled supersaturation field for all particles averaged in time. The dashed line shows the corresponding Gaussian PDF for comparison.

second Damköhler number Da_s in Eq. (7). The corresponding relaxation time τ_s of the passive supersaturation field is of the order of τ_L. All three runs fall into the category of inhomogeneous mixing with $\mathrm{Da}_s \gtrsim 1$, which implies that regions of a cloud are saturated slightly faster than they are mixed by the turbulence. The vapor field is stirred by the fluid turbulence, fluctuations of $s(\boldsymbol{x}, t)$ are effectively sustained in a statistically steady state, and the relaxation timescale $\tau_s \lesssim \tau_L$.

Both Damköhler numbers define an operating point in the parameter plane of our stationary model, $(\mathrm{Da}_s, \mathrm{Da}_d)$. They are shown for the three simulations at different lengths $L = 128$, 256, and 512 mm in Fig. 5. Markers characterize the position of our simulation cases in the Damköhler number space. The solid vertical and horizontal lines characterize the transition from homogeneous to inhomogeneous mixing for both “reaction” processes at $\mathrm{Da} = 1$.

B. Effect of gravity settling and magnitude of constant A_1

In the previous subsection, gravitational settling and droplet inertia were neglected. Their impact is studied now. Similar to previous works [9–11,26], we generalize our droplet dynamics model in the following to one for inertial

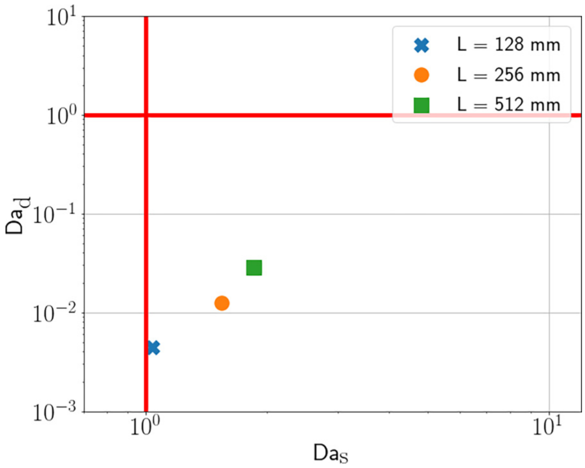

FIG. 5. Parameter space which is spanned by the two Damköhler numbers Da_d and Da_s. The operating points of the three simulation runs are inserted; see the legend and Table I. Solid lines show $\mathrm{Da} = 1$ for both. They mark the corresponding transition between inhomogeneous and homogeneous mixing. Damköhler numbers greater and smaller than 1 characterize inhomogeneous and homogeneous mixing regimes, respectively.

TABLE II. Parameters of the additional simulation runs 2a–2f which have the same setting for the turbulent velocity as run 2. These runs have either a smaller constant A_1 in the transport equation for the supersaturation field or inertia effects included or both. Plus means included; minus means neglected.

Run	A_1 (m^{-1})	r_0 (μm)	Inertia and gravity
2a	5×10^{-4}	10	−
2b	5×10^{-4}	10	+
2c	0.2	20	+
2d	0.2	20	−
2e	5×10^{-4}	20	−
2f	5×10^{-4}	20	+

particles. The Lagrangian equations of motion are then extended to

$$\frac{d\boldsymbol{X}_i}{dt} = \boldsymbol{V}_i, \tag{12a}$$

$$\frac{d\boldsymbol{V}_i}{dt} = \frac{1}{\tau_p^{(i)}}[\boldsymbol{u}(\boldsymbol{X}_i, t) - \boldsymbol{V}_i] - g\boldsymbol{e}_z \tag{12b}$$

for $i = 1, \ldots, n_p$. Here, $\boldsymbol{X}_i$ and $\boldsymbol{V}_i$ are position and velocity for the ith particle, respectively. Time $\tau_p^{(i)} = 2\rho_L r_i^2/(9\rho\nu)$ is the particle response time of the ith droplet, and g is the acceleration due to gravity. To this end, we performed six additional DNSs in the same setting as run 2 of Table I, but with new equations for the particle dynamics; see Eqs. (12). Different combinations of the magnitude of A_1, different initial radii, and droplet inertia are covered by these runs. They are summarized in Table II.

The particle response time τ_p depends on its radius; for particles with a radius $r \approx 20$ μm, the response time is $\tau_p \approx 0.0045$ s. Together with the large-scale eddy turnover time $\tau_L = 2.64$ s as the characteristic velocity field timescale (for runs 2a–2f), the Stokes number $\mathrm{St} = \tau_p/\tau_L \ll 1$. This implies that the Stokes friction term, i.e., the first term on the right-hand side of the particle velocity Eq. (12b), will remain subdominant in comparison to the gravitational settling term, the second term on the right-hand side. Furthermore, a second initial droplet radius of $r_0 = 10$ μm was taken, which leads to different growth rates. Here, inertia effects are even smaller; the radius, however, is still large enough to neglect curvature and hygroscopicity effects for the growth by vapor diffusion of the water droplets [18].

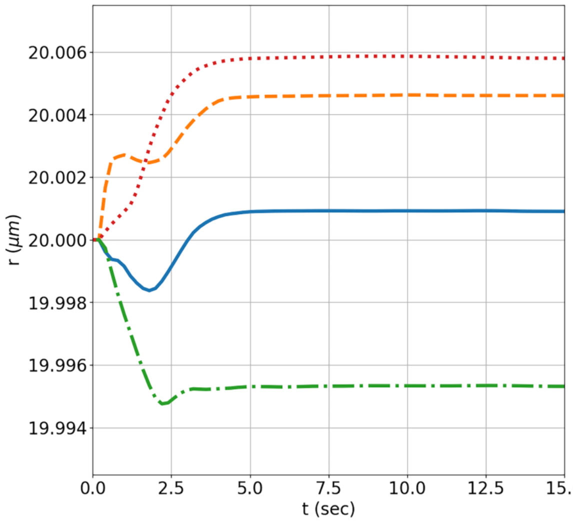

FIG. 7. Droplet radius vs time for four randomly chosen individual droplets in run 2e from Table II.

As seen in Fig. 6, the smaller initial droplet size leads to a faster *relative* growth and shrinking of droplets and thus to a faster relative broadening of the droplet size distribution. Both runs (2a and 2e) were conducted at the corresponding realistic value of $A_1 = 5 \times 10^{-4}$ [8,10]. Thus even at this small A_1, a small change of the droplet size is observed for the short mixing process. After approximately two large-scale eddy turnover times, which correspond to $t \approx 5.3$ s, the mixing process is ceased and the droplet size distribution reaches a steady state, as shown in Fig. 7, where we plot the radius of four selected droplets as a function of time.

The first of the two forcing terms, $A_1 u_z$, in Eq. (3c) keeps the supersaturation field in a statistically steady state; the second term was found to have a very small impact on the dynamics only. With increasing box size and Reynolds number, both terms would gain magnitude and thus enhance the level of fluctuations of the supersaturation field. The present box sizes are too small, such that we decided to enhance the prefactor artificially to keep the supersaturation fluctuations at about $s_{\mathrm{rms}} \approx 2\%$. Increasing A_1 results in an expected faster broadening PDF of droplet radii, as can be seen from Fig. 8. Here, we compared identical simulations with an enhanced

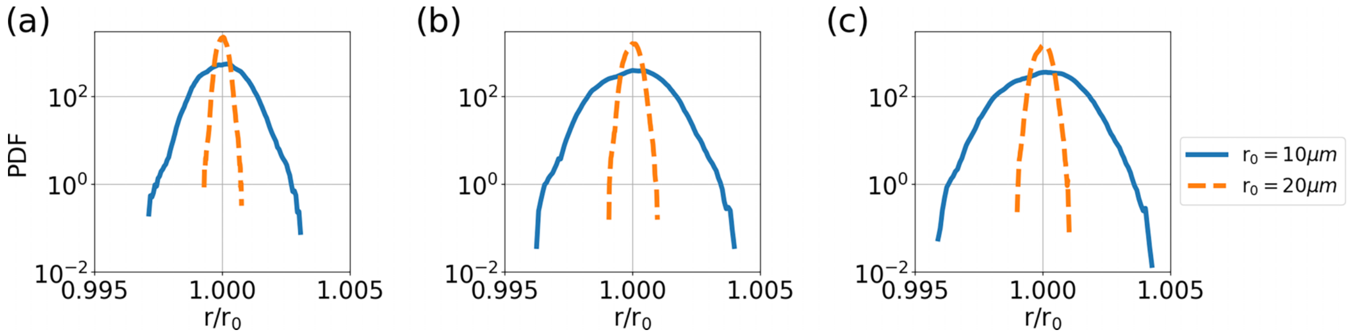

FIG. 6. The impact of different initial sizes of the cloud droplets on the droplet size distribution. Panel (a) is taken at $t = 1$ s, (b) at $t = 2$ s, and (c) $t = 3$ s. Data correspond to runs 2a and 2e in Table II.

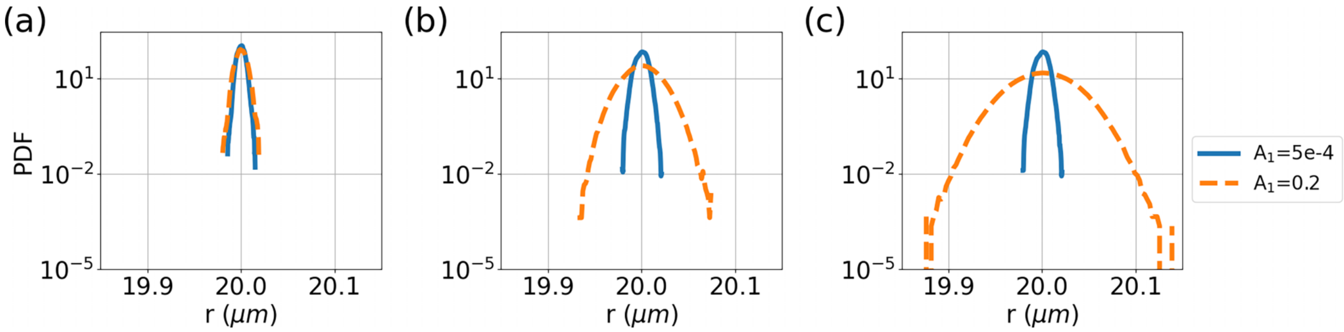

FIG. 8. Comparison of the time evolution of the cloud droplet size distribution for nonenhanced prefactor, $A_1 = 5 \times 10^{-4}$, (solid line) and enhanced factor, $A_1 = 0.2$ (dashed line), for cloud droplets with initial radius $r_0 = 20$ μm. These are runs 2d and 2e from Table II. Panel (a) is taken at $t = 1$ s, (b) at $t = 5$ s, and (c) $t = 15$ s.

$A_1 = 0.2$ to ones with the realistic value for the bulk of a warm cloud, $A_1 \approx 5 \times 10^{-4}$.

Figure 8 reports a further effect, i.e., the longer-term impact of droplet inertia on the broadening of the droplet size distribution for two different initial radii and different A_1. For the initial radius of $r_0 = 10$ μm, the additional impact of inertia, i.e., gravitational settling, remains very small such that the droplet size distributions for droplets with and without inertia collapse almost perfectly for all times reported here and both A_1. This holds even for the tails. In the case of the initial radius of $r_0 = 20$ μm, there is a small effect of the gravitational settling term observable. The gravitational settling term causes a partial decoupling of the droplet tracks from the velocity field and thus from the simultaneously stirred filaments of the supersaturation field. The vertical motion of these bigger droplets is slightly stronger in comparison to the horizontal one. This leads to slightly sparser tails of the droplet size distribution which is visible in all three panels for all three times (see Fig. 9). Sparser tails are also observed when comparing runs 2c and 2d (not shown). The effect becomes visible for the larger $A_1 = 0.2$; it is not detectable for the realistic value of A_1.

V. FINITE-TIME LYAPUNOV EXPONENTS AND SUPERSATURATION

In the Lagrangian approach, the turbulence can be studied along the lines of dynamical systems theory. The deformation of the fluid element assigned with each particle in the turbulent flow can be used to obtain and monitor the local stretching and compression in the flow along droplet trajectories. This information is obtained by means of the finite-time Lyapunov exponents (FTLEs). They are denoted as λ_i with $i = 1, 2, 3$. Applying the gradient of Eq. (4a) with respect to initial condition $X_i(0)$ gives [19,41]

$$\frac{dM_{ij}(t)}{dt} = J_{ik}(t)M_{kj}(t) \quad \text{with} \quad M_{ij}(0) = \delta_{ij}, \tag{13}$$

where $M_{ij} = \partial X_i/\partial X_j(0)$ is the deformation tensor, $J_{ij} = \partial u_i/\partial X_j$ is the Jacobian of the velocity field, and δ_{ij} is the Kronecker delta. Integrating Eq. (13) with respect to time t, which is taken as a multiple integer of the step width Δt, one obtains for the lth particle at the position X_l at time $t = n\Delta t$ a tensor M_{ij} that is given by

$$M^n_{ij} = [\delta_{ik} + J_{ik}|_{X^n_l}\Delta t]M^{n-1}_{kj}. \tag{14}$$

For each time step n, a QR-decomposition of the deformation tensor M_{ij} is performed, i.e.,

$$\hat{M}^n = \hat{Q}^n\hat{R}^n, \tag{15}$$

where $\hat{Q}^n$ is an orthogonal matrix, and $\hat{R}^n$ is the upper-triangle matrix. Since $\hat{Q}^n$ involves only rotations and reflections, the matrix R^n contains information about stretching and compression of the corresponding fluid element, which is assigned with a Lagrangian particle. FTLEs are obtained from the time-averaged exponential growth or decay of the diagonal

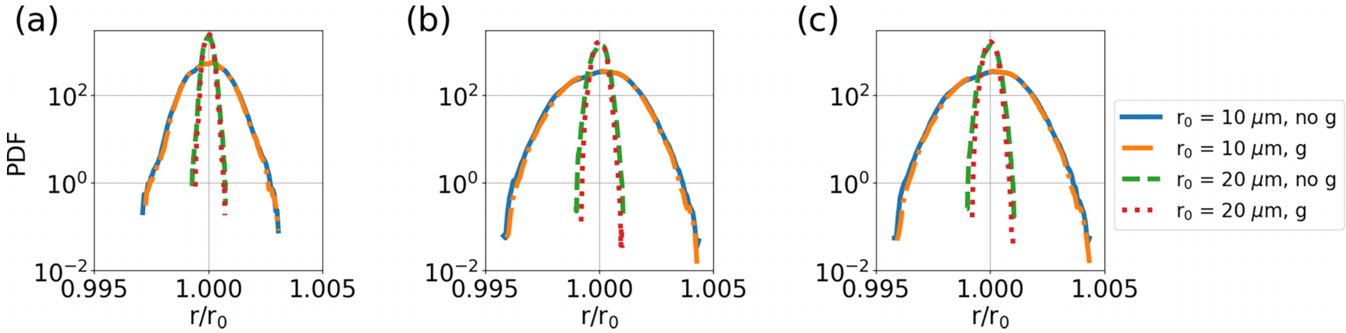

FIG. 9. Comparison of the time evolution of the cloud droplet size distribution for nonenhanced prefactor, $A_1 = 5 \times 10^{-4}$, for cloud droplets with dynamics as gravity settling particles (dash-dotted and dotted lines) and as Lagrangian tracers (solid and dashed lines) for droplets with initial radius $r_0 = 20$ μm (dash-dotted and dashed lines) and $r_0 = 10$ μm (solid and dashed lines). These are runs 2a, 2b, 2e, and 2f from Table II. Panel (a) is taken at $t = 1$ s, (b) at $t = 5$ s, and (c) $t = 15$ s.

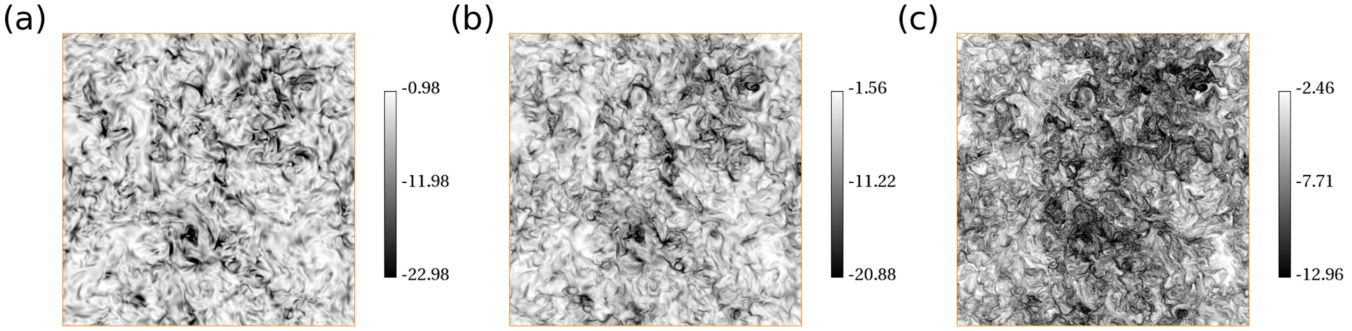

FIG. 10. Contour plots of horizontal slice cuts of $\lambda_3(\boldsymbol{x}, t)$ at different times in units of the large-scale eddy turnover time. (a) $t = 0.03\tau_L$, (b) $t = 0.09\tau_L$, and (c) $t = 0.32\tau_L$. The magnitudes are given by the corresponding color bars. Data are for run 3.

elements, R^n_{ii} (note that no Einstein summation rule is applied here). In detail, the exponents are given by

$$\lambda_i = \frac{1}{n\Delta t}\sum_{j=1}^{n}\ln\left|R^j_{ii}\right|. \tag{16}$$

The FTLEs are then ordered, $\lambda_1 > \lambda_2 > \lambda_3$ for each reference tracer. Since we consider an incompressible flow, the sum of FTLEs follows as

$$\lambda_1 + \lambda_2 + \lambda_3 = 0. \tag{17}$$

The first FTLE λ_1 is always positive and characterizes local stretching, while the intermediate λ_2 can be either negative or positive. The third exponent, λ_3, is always negative and describes the local compression of the fluid element. This exponent characterizes the pile-up of scalar concentration by stirring which can lead to an aggregation of filaments. The evolution of the compression field $\lambda_3(\boldsymbol{x}, t)$ is displayed in Fig. 10. With progressing time the contours get increasingly finer in scale and convoluted. Figure 11 shows the PDFs of all three FTLEs for different moments of time. As can be seen, the PDFs of the FTLEs converge to Gaussian distributions for later times, $t \gtrsim 5\tau_L$. The ratio between mean values of the three FTLEs is seen in Table III. With increasing Reynolds number, the magnitude of all three mean values decreases slightly. The ratio is of approximately the same size as in Ref. [41]. The rates of convergence to the Gaussian case in units of τ_L are approximately the same for the investigated runs, as seen in the figure. We have verified this relaxation by means of the skewness and flatness factors of the PDF(λ_3) which converge to 0 and 3, respectively. The range of Taylor microscale Reynolds numbers R_λ in this study is limited; it basically ends where the range of the studies of Bec *et al.* [42] starts; it is much smaller than in Ref. [41]. This might be why the PDFs for all λ_i become symmetric in our study and do not show the asymmetric form which would follow from the large deviation theory (once the turbulent flows are highly intermittent in the inertial cascade range).

The regions of high compression rates, as characterized by high absolute values of λ_3, describe regions of high turbulent mixing (which means stirring plus diffusion). Thus regions with high magnitudes of λ_3 should also be associated with regions of high spatial variations of the supersaturation field $s(\boldsymbol{x}, t)$, which is probed by the magnitude of the supersaturation gradient or the corresponding scalar dissipation rate; see again Fig. 2. We display the PDFs of the gradient of the supersaturation field (normalized by its rms value) in Fig. 12. The distributions are highly intermittent, as expected. Tails are increasingly extended with growing Reynolds number Re. The far-tail regions are taken as those where $\chi = |\nabla s|/|\nabla s|_{\rm rms} \geqslant 5$.

Figure 13 shows different joint probability density functions (JPDFs). These are $p(\lambda_3, r)$ in panel (a), $p(\lambda_3, s)$ in panel (b), and $p(\lambda_3, \chi)$ in panel (c). Panels (a) and (b) show the typical elliptically shaped contours of the joint PDFs since both distributions are Gaussian. Panel (c) replots the JPDF

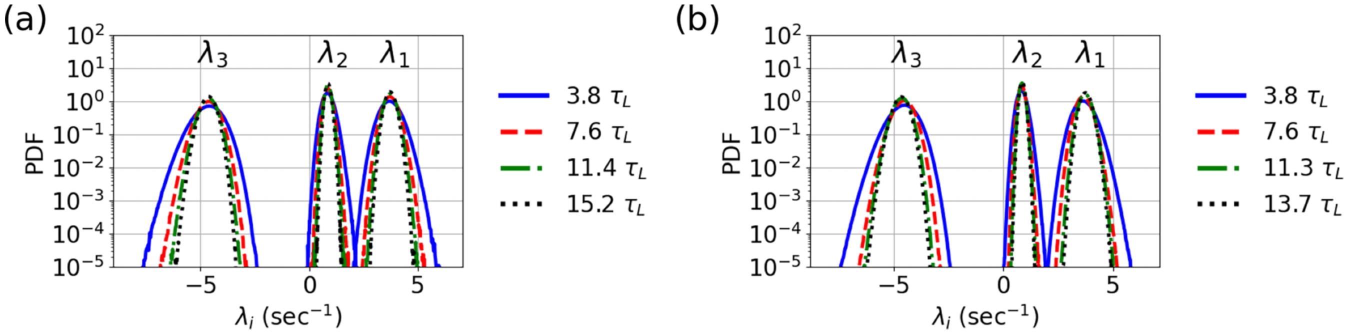

FIG. 11. Probability density functions of the finite-time Lyapunov exponents at different times in units of the large-scale eddy turnover time τ_L. (a) Run 2 with $L = 256$ mm and (b) run 3 with $L = 512$ mm.

TABLE III. Ratio between mean value of FTLE for runs from Table I. The average is taken over all Lagrangian droplet tracks.

Run	$\langle\lambda_1\rangle : \langle\lambda_2\rangle : \langle\lambda_3\rangle$
1	3.8 : 0.9 : −4.7
2	3.7 : 0.9 : −4.6
3	3.7 : 0.8 : −4.5

normalized by the single quantity marginal PDFs,

$$\tilde{p}(\lambda_3, \chi) = \frac{p(\lambda_3, \chi)}{p(\lambda_3)\, p(\chi)}. \tag{18}$$

When the quantity $\tilde{p} > 1$, then the correlation of both statistical quantities is larger as if they were statistically independent. We see that this is exactly the case at the boundary of the support of the JPDF, particularly where larger λ_3 are connected with larger χ. It is expected that this effect becomes stronger when the analysis is moved towards the cloud boundary.

As mentioned above, the FTLEs are used to monitor stretching and compression regions in the turbulent flow. These regions are connected to changes of the supersaturation field. Thus the PDF of λ_3 can be connected to the one of s. Locally, the growth of a filament of the supersaturation can be approximated effectively from a one-dimensional advection by compressive strain [23],

$$S(t) \approx S(t_0)\exp[\lambda_3(t)(t - t_0)], \tag{19}$$

where we define $S(\boldsymbol{x}, t) = s(\boldsymbol{x}, t) + 1$ for convenience. This filament aggregation model [43] is applicable in the crossover region starting from the small-scale end of the inertial range into the viscous range below the Kolmogorov length η_K. This viscous-convective range of passive scalar turbulence is well developed only when Sc $\gg 1$ [23]. Here, the viscous-convective range is narrow (if existing at all). In the crossover range up to scales of a few Kolmogorov lengths η_K, the velocity field should, however, still be sufficiently smooth such that the framework is applicable. Time t_0 in Eq. (19) is the initial time of a time lag over which such a local aggregation process proceeds at many places simultaneously in the bulk of a cloud. The original model of Villermaux and Duplat [21] is formulated for a conserved passive scalar field that is not subject to additional source terms in contrast to the present situation. We incorporate the relative changes of the compression rates $\lambda_3(t)$ relative to t_0 by

$$S(t) \approx S(t_0)\exp\left[\frac{\lambda_3(t)}{\lambda_3(t_0)} - 1\right]. \tag{20}$$

Figure 14 compares the supersaturation PDF for s obtained from the PDF of the compressive FTLE with scalar distribution obtained in DNS. Therefore, we applied the substitution rule

$$P(\tilde{S}) = \int p(\lambda_3, t)\,\delta(\tilde{S} - S(\lambda_3, t))d\lambda_3, \tag{21}$$

where $S(\lambda_3, t)$ follows from (20). As seen, the results obtained from FTLE field show a good agreement with the original analysis of the DNS data. Particularly for later times, the sub-Gaussian tails of the PDF of the supersaturation field are reproduced. A task for future work is to check how well this aggregation model will work when we move towards the edge of the cloud where entrainment processes become important and multiple filament foldings might take place.

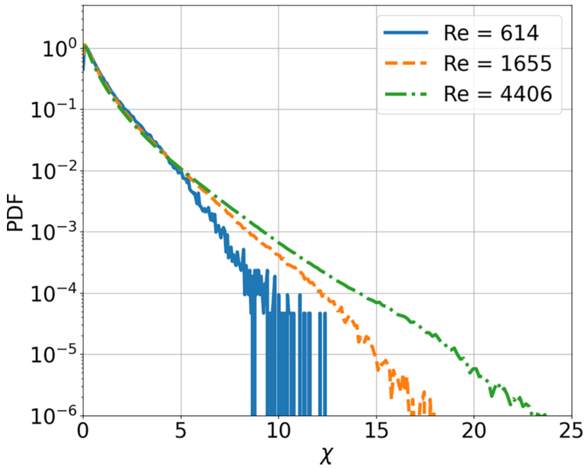

FIG. 12. Probability density function of the magnitude of the gradient of the supersaturation field, $\chi = |\nabla s|/|\nabla s|_{\rm rms}$ for runs 1 (solid line), 2 (dashed line), and 3 (dash-dotted line). We indicate the corresponding Reynolds numbers in the legend.

VI. SUMMARY AND OUTLOOK

In the present work, a simple warm cloud mixing model is presented and analyzed. Instead of two scalar fields—the water vapor mixing ratio q_v and the temperature T—one scalar field, namely the supersaturation s, is used. This supersaturation field contains all required information about water vapor and temperature in the bulk of the cloud and thus determines the evaporation and condensation of cloud droplets [9,10,17]. Direct numerical simulations for the turbulent mixing of the supersaturation field, which is assumed to be a passive scalar field in a homogeneous, isotropic turbulent flow, were performed. For simplicity, we neglected the two-way coupling of the droplets, since the particle Reynolds numbers still remained smaller than 1. Furthermore, we kept the flow in a statistically stationary regime to avoid complex transients, which have been analyzed, for example, in Ref. [20], and which would always be present in a real cloud. The strongly simplified model opened doors for a connection of the supersaturation and droplet statistics to the local strain statistics along Lagrangian trajectories, which is quantified by the FTLEs. Our study is motivated by the aggregation model of turbulent mixing of scalar fields [21,22].

In our model, Eulerian and Lagrangian approaches are combined. The Lagrangian frame is incorporated via the cloud droplets (and thus the liquid water content), which are defined as Lagrangian tracers. Their size depends strongly on the fluctuations of the supersaturation field while they are advected by the turbulent flow. It was shown that the droplet size broadening strongly depends on the Reynolds number. A higher turbulence level triggers larger fluctuations of the supersaturation field and wider distributions of droplet radii. It was also shown that inside the cloud bulk, distributions of droplet radii are Gaussian without extended tails, as found in

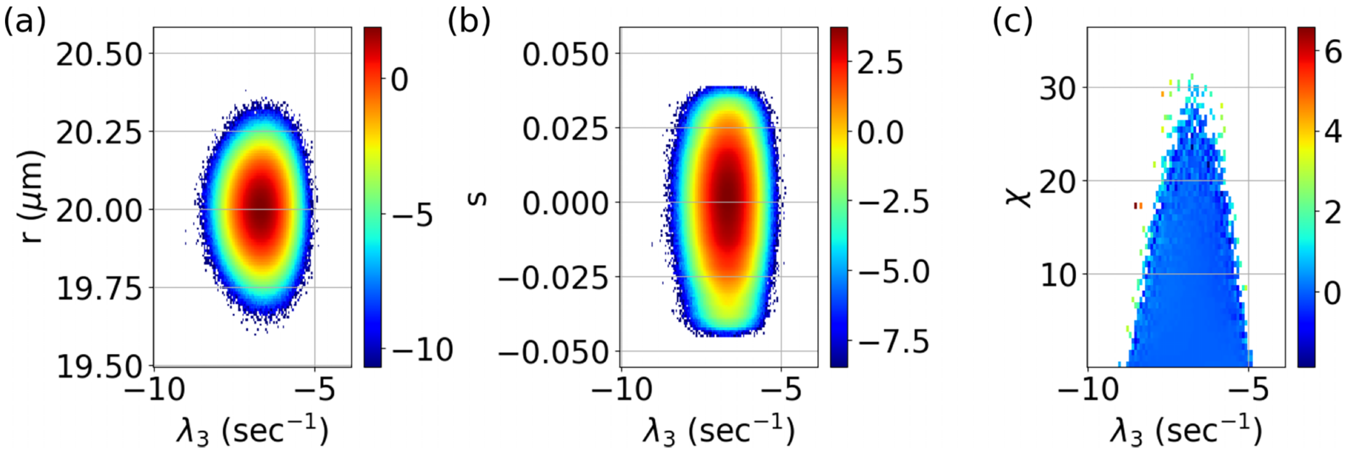

FIG. 13. Joint probability density functions of the third FTLE with (a) the droplet radius, $p(\lambda_3, r)$, (b) the supersaturation field at the particle positions, $p(\lambda_3, s)$, and (c) the normalized gradient magnitude of the supersaturation field, $\tilde{p}(\lambda_3, \chi)$; see (18) for a specific definition. Data are for run 3 at $t = 19.4\tau_L$; see also Fig. 11(b).

entrainment studies [20]. The same holds for the distribution of the supersaturation.

Different mixing regimes have been classified by the Damköhler number. In our DNS, we have an inhomogeneous mixing for the supersaturation field, $\text{Da}_s > 1$. It implies that regions are saturated much faster than they are mixed by the flow. For the droplet evaporation process, a homogeneous mixing regime is obtained for the present parameter settings; in the bulk, droplets experience a rapid change of sub- and supersaturated regions along their pathways, which cause $\text{Da}_d < 1$. See again Fig. 5.

Using the Lagrangian approach allowed us to obtain stretching and compression by calculating FTLE for our Lagrangian tracers. The interdependence of stretching regions defined by the highest absolute values of the third FTLE and regions with the highest supersaturation are obtained from a joint distribution of λ_3 and s. We have seen that the aggregation model of scalar filaments can be applied in principle, similar to [21,23] even though the Schmidt number is Sc $\sim$1. Multiple foldings of scalar filaments, however, are unlikely; the diffusion times are short, and a viscous-convective range of scalar mixing is very small. The statistics of droplet size distribution in the bulk of the cloud remains Gaussian. Furthermore, the small Reynolds numbers of the present cases generated Gaussian distributions of λ_3. At higher Re, intermittency in the inertial cascade range will generate asymmetric distributions in correspondence with large-deviation theory. These studies are currently taken towards the cloud boundary where the entrainment of clear air into cloudy air proceeds and the droplet size distributions develop tails. The results with expected deviations from a Gaussian statistics will be reported elsewhere.

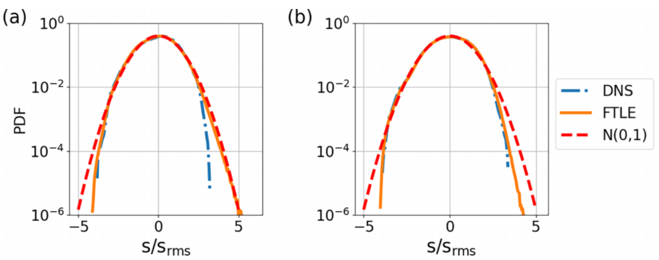

FIG. 14. Probability density functions of supersaturation s for times (a) $t = 4.86\tau_L$ and (b) $t = 9.75\tau_L$, which are obtained from the FTLEs (solid line) from run 3 via the aggregation model. They are compared to the directly evaluated ones (dash-dotted line). The dashed line is a Gaussian PDF.

ACKNOWLEDGMENTS

This work was supported by ITN CoPerMix. The project has received funding from the European Union's Horizon 2020 research and innovation program under the Marie Skłodowska-Curie Grant Agreement No. 956457. Supercomputing time has been provided at the University Computer Center (UniRZ) of the TU Ilmenau. The authors also gratefully acknowledge the Gauss Centre for Supercomputing e.V. [44] for funding this project by providing computing time on the GCS Supercomputer SuperMUC-NG at Leibniz Supercomputing Centre [45]. We thank Priyanka Maity and Dmitry Krasnov for discussions.

APPENDIX: BALANCE EQUATION FOR THE SUPERSATURATION FIELD

In the following, we describe in brief the derivation of the equation of motion of the supersaturation field $s(\boldsymbol{x}, t)$ following the works of Sardina *et al.* [10] and Fries *et al.* [17]. The starting point is the balance equations of the temperature fluctuations $\theta(\boldsymbol{x}, t) = T(\boldsymbol{x}, t) - \langle T(z)\rangle$ and vapor mixing ratio fields $q_v(\boldsymbol{x}, t)$. They are given by

$$\frac{Dq_v}{Dt} = D_v \nabla^2 q_v - C_d, \tag{A1a}$$

$$\frac{D\theta}{Dt} = \kappa \nabla^2 \theta - \frac{g}{c_p} u_z + \frac{L}{c_p} C_d, \tag{A1b}$$

where D_v is the vapor diffusivity, κ is the temperature diffusivity, and C_d is the condensation rate. An additional term that contains the dry adiabatic lapse rate g/c_p is contained in the equation of the temperature fluctuations. In clouds, the lapse rate is somewhat smaller than the dry one, $0.01\ \frac{\mathrm{K}}{\mathrm{m}}$; therefore, even for the largest computation box from Table I with size $L = 0.512$ m, the mean temperature variation does not exceed 0.005 K. Thus the prefactor in the updraft term of the equation for the supersaturation field will have a small prefactor A_1. We are not including a mean updraft of the volume as a whole with a velocity $\langle u_z\rangle$. The condensation rate is given by

$$\begin{aligned} C_d(\boldsymbol{x},t) &= \frac{1}{m_a}\frac{dm_L}{dt} = \frac{4\pi\rho_L}{\rho V_a}\sum_{i=1}^{N} r_i^2\frac{dr_i}{dt} \\ &= \frac{4\pi\rho_L K'}{\rho V_a}\sum_{i=1}^{N} r_i(t)s(\boldsymbol{x}_i,t). \end{aligned} \tag{A2}$$

We will now reduce the two equations to one balance equation, since the supersaturation field summarizes effectively the effects of latent heat release and condensation/evaporation in $q_v(\boldsymbol{x},t)$ and $\theta(\boldsymbol{x},t)$. We start with the material derivative of $s(\boldsymbol{x},t)$, which is given by

$$\frac{Ds}{Dt} = \frac{D}{Dt}\left(\frac{q_v(\boldsymbol{x},t)}{q_{vs}(\boldsymbol{x},t)} - 1\right) = \frac{1}{q_{vs}}\frac{Dq_v}{Dt} - \frac{q_v}{q_{vs}^2}\frac{Dq_{vs}}{Dt}. \tag{A3}$$

First, the material derivative of the saturation mixing ratio (of vapor) q_{vs}, using the ideal gas law, gives

$$\begin{aligned} \frac{Dq_{vs}}{Dt} &= \frac{D}{Dt}\left(\frac{\rho_{vs}}{\rho}\right) = \frac{D}{Dt}\left(\frac{\epsilon e_s}{p}\right) = \frac{\epsilon}{p}\frac{De_s}{Dt} - \frac{\epsilon e_s}{p^2}\frac{Dp}{Dt} \\ &= \frac{\epsilon}{p}\frac{de_s}{d\theta}\frac{D\theta}{Dt} - \frac{\epsilon e_s}{p^2}\frac{Dp}{Dt}, \end{aligned} \tag{A4}$$

where $\varepsilon = R'/R_v$. The total time derivative of the pressure field can be obtained via the hydrostatic equilibrium [46]

$$\frac{Dp}{Dt} = \frac{dp}{dz}\frac{dz}{dt} = -u_z g\rho = -\frac{u_z gp}{R_a\theta}, \tag{A5}$$

where R_a is a gas constant for dry air. By using the Clausius-Clapeyron equation (A5) and (A1b), Eq. (A4) is transformed to

$$\frac{Dq_{vs}}{Dt} = \frac{\epsilon}{p}\frac{Le_s}{R_v\theta^2}\left(\kappa\nabla^2\theta - \frac{g}{c_p}u_z + \frac{L}{c_p}C_d - \frac{\epsilon e_s}{p^2}\frac{u_z gp}{R_a\theta}\right). \tag{A6}$$

Substituting (A6) and (A1a) into (A3) results in

$$\begin{aligned} \frac{Ds}{Dt} &= \frac{1}{q_{vs}}(D_q\nabla^2 q_v - C_d) - \frac{q_v}{q_{vs}^2}\frac{\epsilon}{p}\frac{Le_s}{R_v\theta^2} \\ &\quad\times\left(\kappa\nabla^2\theta - \frac{g}{c_p}u_z + \frac{L}{c_p}C_d - \frac{\epsilon e_s}{p^2}\frac{u_z gp}{R_a\theta}\right). \end{aligned}$$

Thus it follows that

$$\begin{aligned} \frac{Ds}{Dt} &= \frac{1}{q_{vs}}\big(D_q\nabla^2 q_v - C_d\big) - \frac{s+1}{q_{vs}}\frac{\epsilon}{p}\frac{Le_s}{R_v\theta^2} \\ &\quad\times\left(\kappa\nabla^2\theta - \frac{g}{c_p}u_z + \frac{L}{c_p}C_d - \frac{\epsilon e_s}{p^2}\frac{u_z gp}{R_a\theta}\right). \end{aligned}$$

For clouds, supersaturation usually does not exceed 1–2 %. Thus $s \ll 1$ and consequently $s + 1 \approx 1$. Together with the definition of the saturation mixing ratio, one gets

$$\begin{aligned} \frac{Ds}{Dt} &= \frac{pD_q}{\epsilon e_s}\nabla^2 q_v - \frac{p}{\epsilon e_s}\frac{Le_s\kappa}{R_v\theta^2}\nabla^2\theta - C_d \\ &\quad\times\left(\frac{p}{\epsilon e_s} + \frac{p}{\epsilon e_s}\frac{L^2\epsilon e_s}{pR_v\theta^2 c_p}\right) + \frac{Lg}{R_v c_p\theta^2}u_z. \end{aligned} \tag{A7}$$

In the present model, we will approximate diffusion of the supersaturation field as a linear combination of the diffusion processes of temperature and vapor mixing ratio

$$D_s\nabla^2 s = \frac{pD_q}{\epsilon e_s}\nabla^2 q_v - \frac{p}{\epsilon}\frac{L\kappa}{R_v\theta^2}\nabla^2\theta. \tag{A8}$$

The diffusion coefficient of supersaturation is assumed to be equal to the diffusion coefficient of water vapor, $D_s \approx D_q$. Thus the Schmidt number of the scalar supersaturation field will also be $\mathrm{Sc} \approx 0.7$. The coefficient that is connected to the condensation rate can then be transformed in the following way:

$$\frac{p}{\epsilon e_s} + \frac{p}{\epsilon e_s}\frac{L^2\epsilon e_s}{pR_v\theta^2 c_p} = \frac{\rho R'\theta}{\epsilon e_s} + \frac{L^2\epsilon\rho\theta}{p\theta^2 c_p} = \rho\left(\frac{R'\theta}{\epsilon e_s} + \frac{L^2\epsilon}{p\theta c_p}\right). \tag{A9}$$

Substituting (A8), (A9), and (A2) into (A7), we get the final equation for the supersaturation field, which is given by

$$\begin{aligned} \frac{Ds}{Dt} &= D_s\nabla^2 s + \frac{Lg}{R_v c_p\theta^2}u_z - \left(\frac{R'\theta}{\epsilon e_s(\theta)} + \frac{L^2\epsilon}{p\theta c_p}\right)\frac{4\pi\rho_L K}{V_a} \\ &\quad\times\sum_{i=1}^{N} r_i(t)s(\mathbf{x}_i,t). \end{aligned} \tag{A10}$$

The following coefficients can then be defined:

$$A_1 = \frac{Lg}{R_v c_p\theta^2}, \tag{A11a}$$

$$A_2 = \frac{R'\theta}{\epsilon e_s} + \frac{L^2\epsilon}{p\theta c_p}, \tag{A11b}$$

$$K' = \left[\frac{L\rho_L}{K\theta}\left(\frac{L}{R_v\theta} - 1\right) + \frac{\rho_L R_v\theta}{De_s(\theta)}\right]^{-1}. \tag{A11c}$$

Thus the final balance equation of the supersaturation field is

$$\frac{Ds}{Dt} = D_s\nabla^2 s + A_1 u_z - A_2\frac{4\pi\rho_L K'}{V_a}\sum_{i=1}^{N} r_i(t)s(t,\mathbf{x}_i). \tag{A12}$$

This equation couples Eulerian and Lagrangian dynamics and is used in the main text.

[1] R. A. Shaw, Particle-turbulence interactions in atmospheric clouds, Annu. Rev. Fluid Mech. **35**, 183 (2003).

[2] J. R. Norris, R. J. Allen, A. T. Evan, M. D. Zelinka, C. W. O'Dell, and S. A. Klein, Evidence for climate change in the satellite cloud record, Nature (London) **536**, 72 (2016).

[3] A. Kokhanovsky, Optical properties of terrestrial clouds, Earth Sci. Rev. **64**, 189 (2004).

[4] W. W. Grabowski and L.-P. Wang, Growth of cloud droplets in a turbulent environment, Annu. Rev. Fluid Mech. **45**, 293 (2013).

[5] A. M. Blyth, Entrainment in cumulus clouds, J. Appl. Meteorol. **32**, 626 (1993).

[6] J. P. Mellado, Cloud-top entrainment in stratocumulus clouds, Annu. Rev. Fluid Mech. **49**, 145 (2017).

[7] M. Andrejczuk, W. W. Grabowski, S. P. Malinowski, and P. K. Smolarkiewicz, Numerical simulation of cloud–clear air interfacial mixing: Effects on cloud microphysics, J. Atmos. Sci. **63**, 3204 (2006).

[8] A. Celani, A. Mazzino, and M. Tizzi, The equivalent size of cloud condensation nuclei, New J. Phys. **10**, 075021 (2008).

[9] A. S. Lanotte, A. Seminara, and F. Toschi, Cloud droplet growth by condensation in homogeneous isotropic turbulence, J. Atmos. Sci. **66**, 1685 (2009).

[10] G. Sardina, F. Picano, L. Brandt, and R. Caballero, Continuous growth of droplet size variance due to condensation in turbulent clouds, Phys. Rev. Lett. **115**, 184501 (2015).

[11] T. Gotoh, T. Suehiro, and I. Saito, Continuous growth of cloud droplets in cumulus cloud, New J. Phys. **18**, 043042 (2016).

[12] W. W. Grabowski and G. C. Abade, Broadening of cloud droplet spectra through eddy hopping: Turbulent adiabatic parcel simulations, J. Atmos. Sci. **74**, 1485 (2017).

[13] I. Saito and T. Gotoh, Turbulence and cloud droplets in cumulus clouds, New J. Phys. **20**, 023001 (2018).

[14] L. Fossa, S. Abdunabiev, M. Golshan, and D. Tordella, Microphysical time scales and local supersaturation balance at a warm cloud top boundary, Phys. Fluids **34**, 067103 (2022).

[15] W. W. Grabowski, L. Thomas, and B. Kumar, Impact of cloud-base turbulence on CCN activation: Single-size CCN, J. Atmos. Sci. **79**, 551 (2022).

[16] A. Celani, G. Falkovich, A. Mazzino, and A. Seminara, Droplet condensation in turbulent flows, Europhys. Lett. **70**, 775 (2005).

[17] J. Fries, G. Sardina, G. Svensson, and B. Mehlig, Key parameters for droplet evaporation and mixing at the cloud edge, Q. J. R. Meteorol. Soc. **147**, 2160 (2021).

[18] M. K. Yau and R. R. Rogers, *A Short Course in Cloud Physics* (Elsevier, Amsterdam, 1996).

[19] A. Pikovsky and A. Politi, *Lyapunov Exponents: A Tool to Explore complex dynamics* (Cambridge University Press, Cambridge, 2016).

[20] P. Götzfried, B. Kumar, R. A. Shaw, and J. Schumacher, Droplet dynamics and fine-scale structure in a shearless turbulent mixing layer with phase changes, J. Fluid Mech. **814**, 452 (2017).

[21] E. Villermaux and J. Duplat, Mixing as an aggregation process, Phys. Rev. Lett. **91**, 184501 (2003).

[22] J. Duplat and E. Villermaux, Mixing by random stirring in confined mixtures, J. Fluid Mech. **617**, 51 (2008).

[23] P. Götzfried, M. S. Emran, E. Villermaux, and J. Schumacher, Comparison of Lagrangian and Eulerian frames of passive scalar turbulent mixing, Phys. Rev. Fluids **4**, 044607 (2019).

[24] P. Meunier and E. Villermaux, The diffusive strip method for scalar mixing in two dimensions, J. Fluid Mech. **662**, 134 (2010).

[25] P. Meunier and E. Villermaux, The diffuselet concept for scalar mixing, J. Fluid Mech. **951**, A33 (2022).

[26] B. Kumar, J. Schumacher, and R. A. Shaw, Cloud microphysical effects of turbulent mixing and entrainment, Theor. Comput. Fluid Dyn. **27**, 361 (2013).

[27] B. Kumar, F. Janetzko, J. Schumacher, and R. A. Shaw, Extreme responses of a coupled scalar–particle system during turbulent mixing, New J. Phys. **14**, 115020 (2012).

[28] B. Kumar, J. Schumacher, and R. A. Shaw, Lagrangian mixing dynamics at the cloudy-clear air interface, J. Atmos. Sci. **71**, 2564 (2014).

[29] B. Kumar, P. Götzfried, N. Suresh, J. Schumacher, and R. A. Shaw, Scale dependence of cloud microphysical response to turbulent entrainment and mixing, J. Adv. Model. Earth Syst. **10**, 2777 (2018).

[30] C. Siewert, J. Bec, and G. Krstulovic, Statistical steady state in turbulent droplet condensation, J. Fluid Mech. **810**, 254 (2017).

[31] M. Pinsky, A. Khain, and A. Korolev, Theoretical analysis of mixing in liquid clouds–part 3: Inhomogeneous mixing, Atmos. Chem. Phys. **16**, 9273 (2016).

[32] F. Burnet and J.-L. Brenguier, Observational study of the entrainment-mixing process in warm convective clouds, J. Atmos. Sci. **64**, 1995 (2007).

[33] J. B. Jensen and M. B. Baker, A simple model of droplet spectral evolution during turbulent mixing, J. Atmos. Sci. **46**, 2812 (1989).

[34] M. A. Beals, J. P. Fugal, R. A. Shaw, J. Lu, S. M. Spuler, and J. L. Stith, Holographic measurements of inhomogeneous cloud mixing at the centimeter scale, Science **350**, 87 (2015).

[35] K. K. Chandrakar, W. Cantrell, S. Krueger, R. A. Shaw, and S. Wunsch, Supersaturation fluctuations in moist turbulent Rayleigh-Bénard convection: A two-scalar transport problem, J. Fluid Mech. **884**, A19 (2020).

[36] J. Schumacher, K. R. Sreenivasan, and V. Yakhot, Asymptotic exponents from low-Reynolds-number flows, New J. Phys. **9**, 89 (2007).

[37] D. Pekurovsky, P3DFFT: A framework for parallel computations of fourier transforms in three dimensions, SIAM J. Sci. Comput. **34**, C192 (2012).

[38] A. Celani, A. Lanotte, A. Mazzino, and M. Vergassola, Fronts in passive scalar turbulence, Phys. Fluids **13**, 1768 (2001).

[39] D. Kushnir, J. Schumacher, and A. Brandt, Geometry of intensive scalar dissipation events in turbulence, Phys. Rev. Lett. **97**, 124502 (2006).

[40] K. K. Chandrakar, W. Cantrell, K. Chang, D. Ciochetto, D. Niedermeier, M. Ovchinnikov, R. A. Shaw, and F. Yang, Aerosol indirect effect from turbulence-induced broadening of cloud-droplet size distributions, Proc. Natl. Acad. Sci. (USA) **113**, 14243 (2016).

[41] P. L. Johnson and C. Meneveau, Large-deviation joint statistics of the finite-time Lyapunov spectrum in isotropic turbulence, Phys. Fluids **27**, 085110 (2015).

[42] J. Bec, L. Biferale, G. Boffetta, M. Cencini, S. Musacchio, and F. Toschi, Lyapunov exponents of heavy particles in turbulence, Phys. Fluids **18**, 091702 (2006).

[43] E. Villermaux and J. Duplat, Mixing is an aggregation process, C. R. Mecanique **331**, 515 (2003).

[44] https://www.gauss-centre.eu.

[45] https://www.lrz.de.

[46] H. R. Pruppacher, J. D. Klett, and P. K. Wang, *Microphysics of Clouds and Precipitation* (Springer, Heidelberg, 2010).